Materials Today Sustainability 34 (2026) 101348

Contents lists available at ScienceDirect

Materials Today Sustainability

journal homepage: www.journals.elsevier.com/materials-today-sustainability

The rational design of $Au^0/g\text{-}C_3N_4$ photocatalysts with enhanced charge separation for visible-light-driven water purification

Mshaal Almalki *, Ouardia Akdim, James S. Hayward, Jennifer K. Edwards, Jonathan K. Bartley **

Cardiff Catalysis Institute, School of Chemistry, University of Cardiff, Cardiff, CF10 3AT, UK

ARTICLE INFO

Keywords:
Graphitic carbon nitride
photocatalysis
methyl orange degradation

ABSTRACT

Gold nanoparticle doped graphitic carbon nitride ($Au/g\text{-}C_3N_4$) photocatalysts were synthesized via different preparation methods and evaluated for the visible-light-driven degradation of methyl orange at room temperature. All Au-modified samples exhibited superior photocatalytic activity compared to unmodified $g\text{-}C_3N_4$, which was attributed to the positive role of gold in enhancing charge separation. Notably, catalysts containing well-dispersed Au bimodal size distribution (<0.5 nm intercalated between the layers and 2 nm on the surface) displayed the highest efficiency, achieving complete methyl orange degradation within 180 min. The superior activity of the simple impregnation-derived sample was attributed to its small Au particle size and strong interaction with the $g\text{-}C_3N_4$ matrix, which facilitated electron trapping and reactive oxygen species generation as shown by photoluminescence, photocurrent response and electrochemical impedance spectroscopy Nyquist plots. The degradation mechanism was determined based on radical scavenger experiments and the dominant reactive species observed were superoxide radicals ($O2^{\bullet-}$), hydroxyl radicals ($^{\bullet}OH$), and photogenerated holes (h^+). The solution pH was found to significantly influence the initial adsorption of methyl orange onto the catalyst surface, thereby affecting the overall degradation process. Among the tested strategies, incipient wetness and impregnation routes emerged as promising, facile approaches for the preparation of efficient photocatalysts. This work highlights how synthesis methodology critically governs the physicochemical properties and photocatalytic performance of $Au/g\text{-}C_3N_4$, offering valuable insights for the design of photocatalysts as sustainable materials for water purification.

1. Introduction

Recently, the utilization of visible light in green technologies has gained increasing attention as a sustainable strategy to tackle environmental challenges and energy shortages. Photocatalysis driven by visible light, particularly employing semiconductor materials, has emerged as an efficient approach for renewable energy generation and environmental remediation [1,2]. In this process, semiconductors absorb photons to generate charge carriers that participate in redox reactions, enabling hydrogen production from water and the degradation of organic pollutants [3]. A wide range of semiconductors—including TiO_2, ZnO, CoS, perovskites ABO_3 (e.g., $BiFeO_3$, $BaTiO_3$, $SrTiO_3$), and ABO_4 compounds (e.g., $ZnWO_4$, $SnWO_4$)—have been investigated for such applications [4,5]. However, many of these possess wide band gaps (>3.2 eV), restricting absorption mainly to the ultraviolet region, which accounts for less than 4% of the solar spectrum [6]. This limitation has motivated the search for narrower band-gap materials capable of more effectively harnessing visible light [4]. Among the promising candidates, graphitic carbon nitride ($g\text{-}C_3N_4$), an organic semiconductor, has recently attracted significant attention due to its visible-light activity, low cost, and environmental stability [1,2,4,7]. It can be synthesised from abundant nitrogen-rich precursors (cyanamide, melamine, dicyandiamide, urea, or thiourea) via thermal polymerization, forming a polymeric material with graphitic stacking of C_3N_4 layers constructed from tri-s-triazine units linked by planar amino groups (Fig. 1) [7–9].

Graphitic carbon nitride possesses a suitable bandgap of 2.7 eV (460 nm) for visible light response, a high heat resistance temperature of up to 600 °C, high chemical stability during photocatalysis in aqueous solutions, and is characterized by strong covalent bonds between carbon and nitrogen atoms [10]. Additionally, it is nontoxic and can be

* Corresponding author.
** Corresponding author.
E-mail addresses: AlmalkiMA1@cardiff.ac.uk (M. Almalki), BartleyJK@cardiff.ac.uk (J.K. Bartley).

https://doi.org/10.1016/j.mtsust.2026.101348
Received 30 December 2025; Received in revised form 27 February 2026; Accepted 15 March 2026
Available online 16 March 2026

fabricated from different precursors using simple, cost-effective synthesis methods [10]. Despite these advantages, pure g-C_3N_4 exhibits drawbacks such as facile electron–hole recombination, low surface area, and low quantum efficiency [11]. To overcome these limitations and enhance the photocatalytic efficiency of g-C_3N_4, it is imperative to reduce the recombination rate between electrons and holes, increase the surface area, and broaden the absorbed light region. One promising approach to improve the photocatalytic performance of g-C_3N_4 involves creating composite materials by combining g-C_3N_4 with precious metals such as Au and Ag, a strategy that has yielded positive results [2,11]. The addition of Au and Ag nanoparticles on the surface of g-C_3N_4 enhance the separation of electron–hole pairs, acting as electron traps to prevent electron–hole pair recombination and thereby improving photocatalytic efficiency [12–14].

To date, various chemical reduction methods have been employed to load noble metal nanoparticles (NPs) onto the surface of g-C_3N_4 nanomaterials [12,15]. However, the majority of noble/g-C_3N_4 composites were effectively synthesised with the aid of surfactants, chemical reducing agents or under photoreduction [9,16,17]. Methyl orange (MO) was selected as a model organic pollutant due to its widespread use as an azo dye in textile and printing industries and its persistence in aquatic environments [18]. Azo dyes represent one of the largest classes of industrial colorants discharged into wastewater and are resistant to conventional treatment processes [18]. Therefore, the photocatalytic degradation of MO serves as a representative reaction to evaluate the potential of visible-light photocatalysts for sustainable water remediation and as this is a widely studied reaction it can be used to benchmark the performance of our catalysts.

In this study, different synthesis techniques were investigated to prepare 1 wt% Au/g-C_3N_4 materials, which were evaluated as catalysts for methyl orange (MO) degradation. It was found that the simple and scalable incipient wetness method, which does not require a sacrificial reducing agent or high temperature post treatment, delivered superior photocatalytic performance compared to methods involving the addition of a sacrificial reducing agent.

2. Experimental

2.1. Catalyst preparation

All chemical reagents were analytical grade and used without further purification, with a full list given in Table S1. Deionized (DI) water was used throughout for all the experiments.

2.1.1. Synthesis of bare (g-C_3N_4)

Bulk g-C_3N_4 was prepared by placing 30 g of urea in an alumina crucible with a lid and calcining in a muffle furnace, at 550 °C for 3 h with a heating rate of 3 °C min^{-1}.

2.1.2. Synthesis methods for producing 0.2 g of 1 wt% Au/g-C_3N_4

2.1.2.1. Incipient wetness (IW) method. DI water was added dropwise to 0.198 g of g-C_3N_4 until a consistency paste was obtained, followed by the addition of 161.2 µL of aqueous $HAuCl_4$ solution (12.4 g L^{-1}). The resulting paste was then dried in air at 90 °C for 18 h. The obtained catalyst was ground in a pestle and mortar before use.

2.1.2.2. Washed incipient wetness (WIW) method. DI water was added dropwise to 0.198 g of g-C_3N_4 until a paste like consistency was achieved, followed by the addition of 161.2 µL of aqueous $HAuCl_4$ solution (12.4 g L^{-1}). The resulting paste was then dried in air at 90 °C for 18 h. The next day, the catalyst was washed twice with 20 mL deionized water, followed by one wash with 20 mL ethanol, and then dried in air at 90 °C for 16 h. The obtained catalyst was ground in a pestle and mortar before use.

2.1.2.3. Impregnation (Im) method. 0.198 g of g-C_3N_4 was dispersed in 20 mL DI water and left under ultrasonication for 1 h at room temperature. 161.2 µL of $HAuCl_4$ solution (12.4 g L^{-1}) was then added and the suspension was stirred at room temperature for 18 h. The sample was then centrifuged (4350 rpm) for 30 min, to collect the solid phase. The catalyst was then washed twice with 20 mL deionized water, followed by one wash with 20 mL ethanol, and then dried in air at 90 °C for 16 h. The obtained catalyst was ground in a pestle and mortar before use.

2.1.2.4. Impregnation with reducing agent (RA) method. 0.198 g of g-C_3N_4 was dispersed in 20 mL of DI water and ultrasonicated for 1 h at room temperature. 161.2 µL of $HAuCl_4$ solution was then added and the suspension was stirred at room temperature for 15 min. A $NaBH_4$ solution (0.1 mol L^{-1}) was freshly prepared in an ice bath (0-4 °C) to minimize decomposition and maintain reducing capacity and used as the reducing agent, with a $NaBH_4$/metal molar ratio of 5. Subsequently, 0.5 mL of the $NaBH_4$ solution was rapidly injected into the suspension,

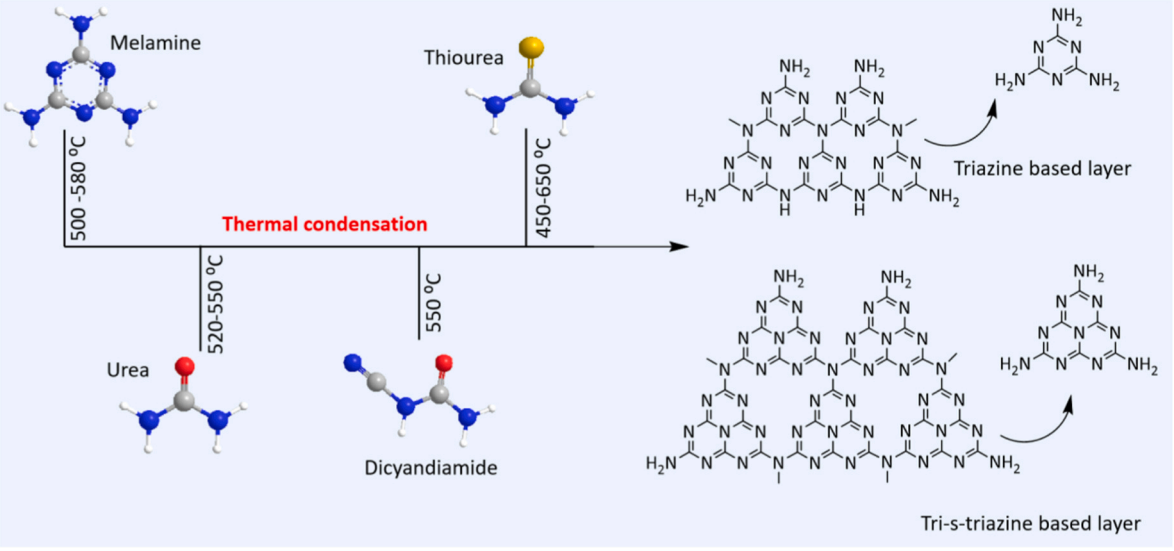

Fig. 1. Molecular structures of g-C_3N_4 precursors along with their thermal polycondensation temperatures, illustrating triazine and tri-s-triazine as possible g-C_3N_4 allotropes. Original figure with structural information adapted from Refs. [7–9].

which was then stirred for 2 h. The sample was then centrifuged (4350 rpm) for 30 min, to collect the solid phase. The catalyst was then washed twice with 20 mL deionized water, followed by one wash with 20 mL ethanol, and then dried in air at 90 °C for 16 h. The obtained catalyst was ground in a pestle and mortar before use.

2.1.2.5. Sol immobilisation (SIm) method. 161.2 μL of $HAuCl_4$ solution was dispersed in 20 mL of DI water under vigorous stirring at room temperature. Then, 0.26 mL of polyvinyl alcohol (PVA) (1 wt%) was added to give a PVA/metal molar ratio of 1.3 and the resulting suspension was stirred for 15 min. A freshly prepared $NaBH_4$ solution (0.1 mol L^{-1}, prepared in an ice bath) was used as the reducing agent, with a $NaBH_4$/Au molar ratio of 5. Subsequently, 0.5 mL of the $NaBH_4$ solution was rapidly injected into the suspension, which was then stirred for 30 min before the addition of g-C_3N_4 (0.198 g). The suspension was then filtered under vacuum and washed with deionized water (20 mL) and then dried 16 h at 90 °C. The obtained catalyst was ground in a pestle and mortar before use.

2.2. Materials characterisation

The crystalline phases of the prepared materials were examined by X-ray diffraction (XRD) using a PANalytical X'Pert Pro powder diffractometer operated at 40 kV and 40 mA with Cu Kα radiation (λ = 1.54 Å) and a Ge (111) single crystal monochromator. Phase identification was carried out with reference to the International Centre for Diffraction Data (ICDD) database.

Transmission electron microscopy (TEM) was performed on a JEOL JEM-2100 microscope operating at 200 kV. Samples were prepared by dispersing powders onto 300-mesh copper grids coated with a holey carbon film.

The textural properties were evaluated by N_2 adsorption–desorption isotherms collected on a Quantachrome Nova 2200 E analyzer. Surface areas were calculated using the Brunauer–Emmett–Teller (BET) model. Prior to measurements, samples were dried at 150 °C for 2 h and subsequently outgassed under vacuum.

The surface chemical composition was investigated by X-ray photoelectron spectroscopy (XPS) using a Thermo Fisher Scientific K-Alpha$^+$ spectrometer with monochromatic Al Kα radiation (72 W, 6 mA × 12 kV) and operated in 400 μm spot mode (analysis area ca. 400 × 600 μm), with a reference C 1s binding energy of 285 eV. Surface atomic concentrations were determined from transmission-corrected spectra using Scofield sensitivity factors and electron inelastic mean free paths calculated using the TPP-2M model, following Shirley background subtraction.

The bulk Au content of the samples was quantified by microwave plasma–atomic emission spectroscopy (MP-AES) using an Agilent 4200 MP-AES system. Prior to analysis, 50 mg of catalyst was digested in 5 mL of aqua regia for 24 h, followed by dilution to a metal concentration of ~10 ppm. The Au loading was expressed as weight percent (wt.%).

To investigate potential Au leaching from the support, the post-reaction solution was analyzed by ICP-MS using an Agilent 7900 instrument. Prior to ICP-MS analysis, samples were digested in aqua regia.

The optical absorption properties were characterized using a CARY 4000 UV–Vis spectrophotometer fitted with a Harrick Praying Mantis diffuse reflectance attachment. Measurements were recorded over the range of 200–800 nm, with $BaSO_4$ (99.998%, Sigma Aldrich) serving as the reflectance standard.

Photoluminescence (PL) spectra were recorded on an F98 fluorescence spectrophotometer (Shanghai Lengguang Technology Co.) at an excitation wavelength of 350 nm.

Photoelectrochemical measurements were conducted using a Bio-Logic SP-150 potentiostat analyzer with a three-electrode configuration. Further experimental details are provided in the supplementary information.

2.3. Evaluation of photocatalytic performance

MO photodegradation was carried out in a photoreactor under visible light with wavelengths in the range 400–700 nm, using a SOLIS-3C actual-power LED lamp (Thorlabs, 68 mW cm^{-2}). In a typical experiment, 25 mg of catalyst was suspended in 50 mL of MO solution (10 mg L^{-1}) to give a catalyst concentration of 500 mg L^{-1}. Before the photocatalytic degradation the solution was kept in the dark under sonication for 15 min to reach the adsorption-desorption equilibrium. The solution was then exposed to the light under magnetic stirring (350 rpm) at room temperature. At defined timepoints, 1 mL of the solution was collected, and passed through a 0.45 μm pore size syringe filter before analysis. The absorbance was measured at 464 nm using a UV-Vis Spectrophotometer (Agilent Technologies) in the range 200–800 nm and compared to a calibration curve.

The photocatalytic efficiency of each tested catalyst was estimated by using the following equation:

$$\text{Degradation Efficiency } (\%) = [1\text{-} (C_t/C_0)] \times 100 \quad (1)$$

Where C_0 and C_t represent the initial and remaining concentration of the dye at time of exposure t.

3. Results and discussion

3.1. Characterization of materials

Following synthesis, the physiochemical properties of the Au/g-C_3N_4 catalysts were determined using several complimentary techniques. The surface area and the Au loading of the synthesised g-C_3N_4-based photocatalysts was measured by ICP-MS and shown in Table 1.

The specific surface areas of the unmodified g-C_3N_4 and the Au-loaded catalysts are summarized in Table 1 with the full isotherms and pore size distributions shown in Fig. S1 and Table S2. Pristine g-C_3N_4 exhibited a surface area of 39 ± 3 m^2 g^{-1}, which is consistent with literature values for bulk carbon nitride prepared via thermal polymerization [19]. Upon gold deposition, all catalysts displayed surface areas of 45–50 m^2 g^{-1}, indicating the minimal influence of the Au loading (1 wt%) and preparation method on the g-C_3N_4 surface area. Although the nominal gold loading was fixed at 1.0 wt% across all synthetic routes, ICP-MS analysis revealed small variations in the actual loadings, reflecting differences in gold deposition efficiency among the methods. The incipient wetness (IW) catalyst and the sol immobilisation (Sim) catalyst both closely matched the intended loading. The high Au loading obtained with the incipient wetness impregnation method is typical as the low volume of water allows all of the gold to be deposited on the support and does not include a washing step that can remove the metal. The other methodologies rely on favourable interactions between the precursors in solution and the g-C_3N_4 to deposit them on the support. Although this was successful in giving a high loading of gold in the SIm catalyst, the impregnation (Im) catalyst and the catalyst prepared with the addition of a reducing agent (RA) displayed somewhat reduced Au

Table 1
Specific surface area, determined by BET of g-C_3N_4-based photocatalysts, and Au actual loading determined by ICP-MS of the AR-digested samples for 1 wt% Au/g-C_3N_4.

Sample Name	BET specific surface area (m^2 g^{-1})	Nominal Loading (wt%)	Actual loading (wt%)
g-C_3N_4	39 ± 3	-	-
IW	45 ± 2	1.0	1.05 ± 0.05
Im	48 + 4	1.0	0.90 ± 0.11
RA	46 + 2	1.0	0.85 ± 0.16
SIm	45 ± 1	1.0	0.99 ± 0.05

contents, at 0.90 ± 0.11 wt% and 0.85 ± 0.16 wt%, respectively. These deviations are likely to be due to incomplete adsorption of the Au precursor from the solution or partial loss during the washing and reduction steps associated with these methods. These results highlight that while all four deposition routes yielded Au/g-C_3N_4 catalysts with similar textural properties, their efficiency in incorporating gold varied, confirming that the deposition method significantly affects metal retention.

Fig. 2 shows the TEM images and particle size distributions of the Au/g-C_3N_4 catalysts prepared by the different deposition methods. All samples display thin g-C_3N_4 layers supporting Au nanoparticles (NPs). The IW and Im catalysts (Fig. 2a and b) exhibit uniformly dispersed Au NPs with mean diameters of 2.5 ± 0.2 nm and 2.3 ± 0.1 nm, respectively. In contrast, the RA method using $NaBH_4$ produced significantly larger Au particles, with a mean size of 12.5 ± 0.8 nm (Fig. 2c). For the SIm catalyst (Fig. 2d), Au nanoparticles were homogeneously distributed across g-C_3N_4 with a moderate mean size of 4.5 ± 0.2 nm, attributed to the stabilising effect of polyvinyl alcohol (PVA) prior to $NaBH_4$ reduction. These results clearly demonstrate that the deposition route has a pronounced influence on both the size and loading of Au nanoparticles. While IW and Im methods favour the formation of small nanoparticles with a narrow particle size distribution, RA leads to uncontrolled growth of larger particles, and SIm achieves intermediate particle sizes with uniform dispersion due to the presence of a stabiliser.

X-ray diffraction patterns of the synthesised catalysts are shown in Fig. 3. All the samples exhibit diffraction peaks at around 12.8° and 27.5°, associated with the (001) and (002) planes of the g-C_3N_4, according to the JCPDS card No. 87-1526 [17]. The (001) plane is associated with the repetitive in-planar tris-s-triazine structured packing (heptazine units), while the (002) plane corresponds to the interlayer stacking of the heptazine network, as shown in Fig. 3a [20]. A detailed examination of the XRD patterns within the 2θ angle range of 22–36° provided further insights into the (002) peak diffraction of g-C_3N_4 (Fig. 3b). The IW and Im catalysts displayed reduced 2θ values (27.2°) compared to bare g-C_3N_4 (27.71°). Using Bragg's equation ($n\lambda = 2d \sin\theta$, where $\lambda = 1.54$ Å for Cu Kα radiation), the interlayer d-spacing was calculated to increase from 0.32 to 0.33 nm ($\Delta d \approx 0.01$ nm) [21]. Given that this expansion is insufficient to accommodate the ~2 nm Au nanoparticles observed by TEM, the peak shift may more reasonably be attributed to local structural distortion and partial disruption of the π–π stacked g-C_3N_4 layers induced by ultrasmall Au clusters (<0.5 nm) or atomically dispersed Au (below the detection limit of conventional TEM) [21,22]. The diffraction angle 2θ of 33–80° (Fig. 3c) shows the presence of Au on the g-C_3N_4 for the RA and SIm catalysts. The catalyst prepared by RA, exhibits typical peaks of Au crystals with peaks at 38.2° and 44.6°, which are indexed to the (111), and (200) planes, respectively, according to the JCPDS No. 4-0783. Similarly, the SIm catalyst displays the same peaks, though with broader profiles. These peaks confirm the face-centred cubic (FCC) structure of the Au NPs [23]. Notably, no Au diffraction peaks were detected for IW and Im catalysts due to ultrasmall Au species (<0.5 nm and ~2 nm by TEM, below XRD detection limit of ~3-5 nm) and their high dispersion and possible subsurface or defect-associated distribution within the g-C_3N_4 framework [21,22,24].

X-ray photoelectron spectroscopy (XPS) measurements were performed to investigate the chemical states of carbon, nitrogen, and oxygen on the g-C_3N_4 and Au/g-C_3N_4 catalysts. All spectra were calibrated using the C–C peak at 285.0 eV as the reference. As shown in Fig. 4a, the XPS survey spectra confirm the presence of C, N, and O, with no additional impurity signals were detected. A very weak O 1s peak at ~530 eV is observed, attributed to surface-adsorbed oxygen species, due to adsorbed H_2O or O_2 from the atmosphere [25]. The N 1s high-resolution spectra (Fig. 4b) exhibit three distinct peaks. The dominant peak at 398.66 eV is assigned to the –C=N– bonded nitrogen atom in the triazine ring. Two additional components at 400.33 eV and 404.5 eV are attributed to nitrogen atoms bonded to three-carbon atoms ([N–$(C)_3$]), C=N–C structures, amino groups, and π-excitation. Comparatively, all Au-loaded samples show a reduction in the intensity of the 398.8 eV peak, which may indicate, partial disruption of the g-C_3N_4 framework due to Au nanoparticle interaction, which is most pronounced for the SIm catalyst, indicating surface coverage by PVA (used in SIm synthesis), may block or alter N-rich sites [15,26,27]. On the C 1s high-resolution spectra of g-C_3N_4 and Au/g-C_3N_4 samples (Fig. 4c), the two peaks at ~288.36 and 285.0 eV, correspond to the N–C=N bonds of g-C_3N_4 backbone, and to C–C bonds of the adventitious carbon, respectively. The satellite structure of these rings give rise to a second feature, centred around 293.2 eV. A decrease in the N-C=N intensity was observed for the catalysts following Au addition, which is probably due to the interaction of the Au NPs, that can alter the electronic

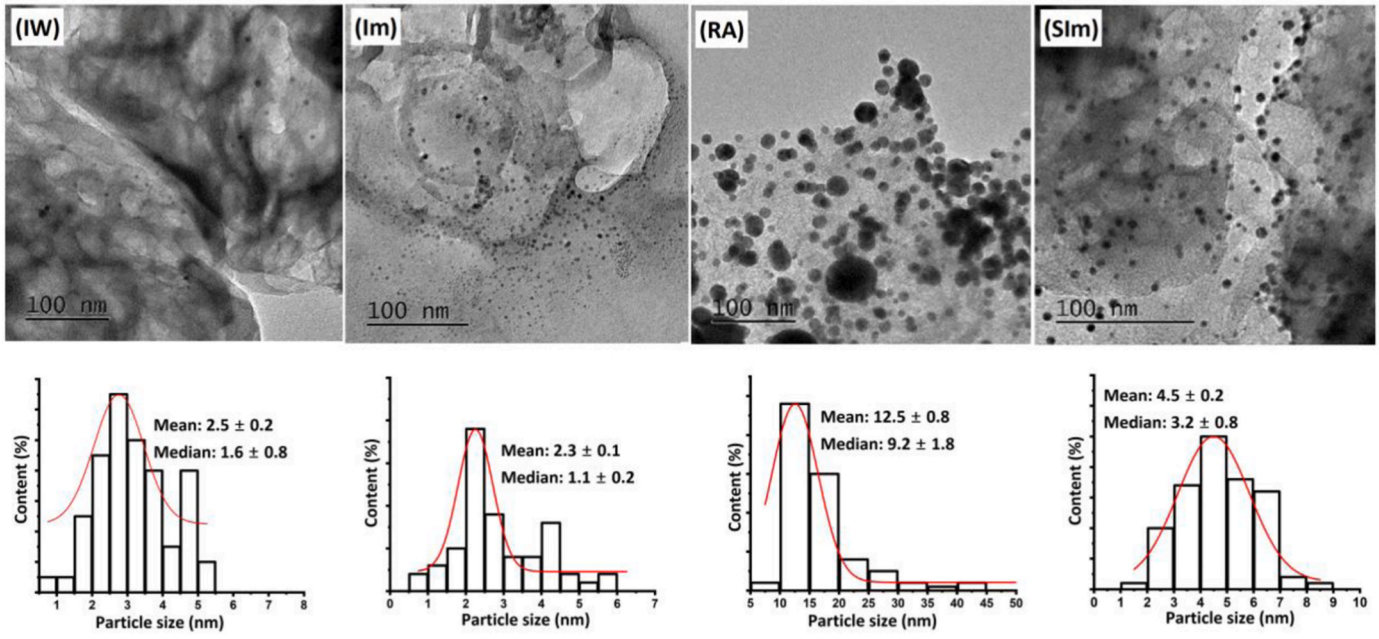

Fig. 2. Representative TEM images and corresponding particle size distributions for the 1 wt% Au/g-C_3N_4 samples synthesised using different preparation techniques. Key: IW = incipient wetness, Im = impregnation, RA = impregnation in the presence of a reducing agent; SIm = Sol immobilisation.

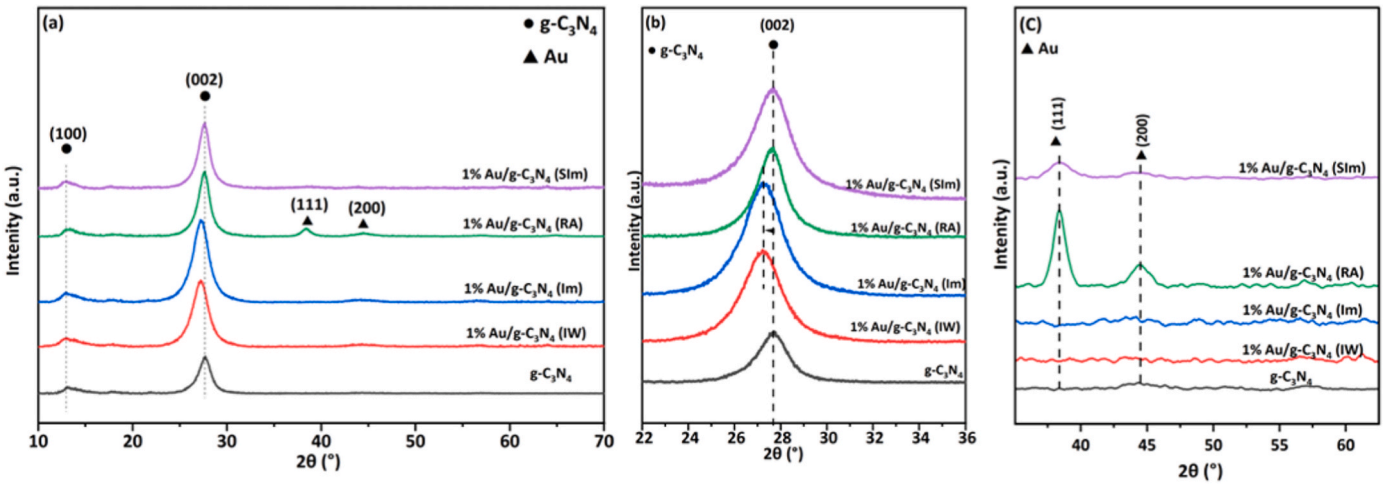

Fig. 3. XRD diffraction patterns of: (a) the 1 wt% Au/g-C_3N_4 samples synthesised using different preparation techniques compared to the unmodified g-C_3N_4; (b) the enlarged view of the g-C_3N_4 (002) peak; and (c) the XRD patterns from 33° to 80° showing the (111) and (200) reflections Au nanoparticles. Key: IW = incipient wetness, Im = impregnation, RA = impregnation in the presence of a reducing agent; SIm = Sol immobilisation.

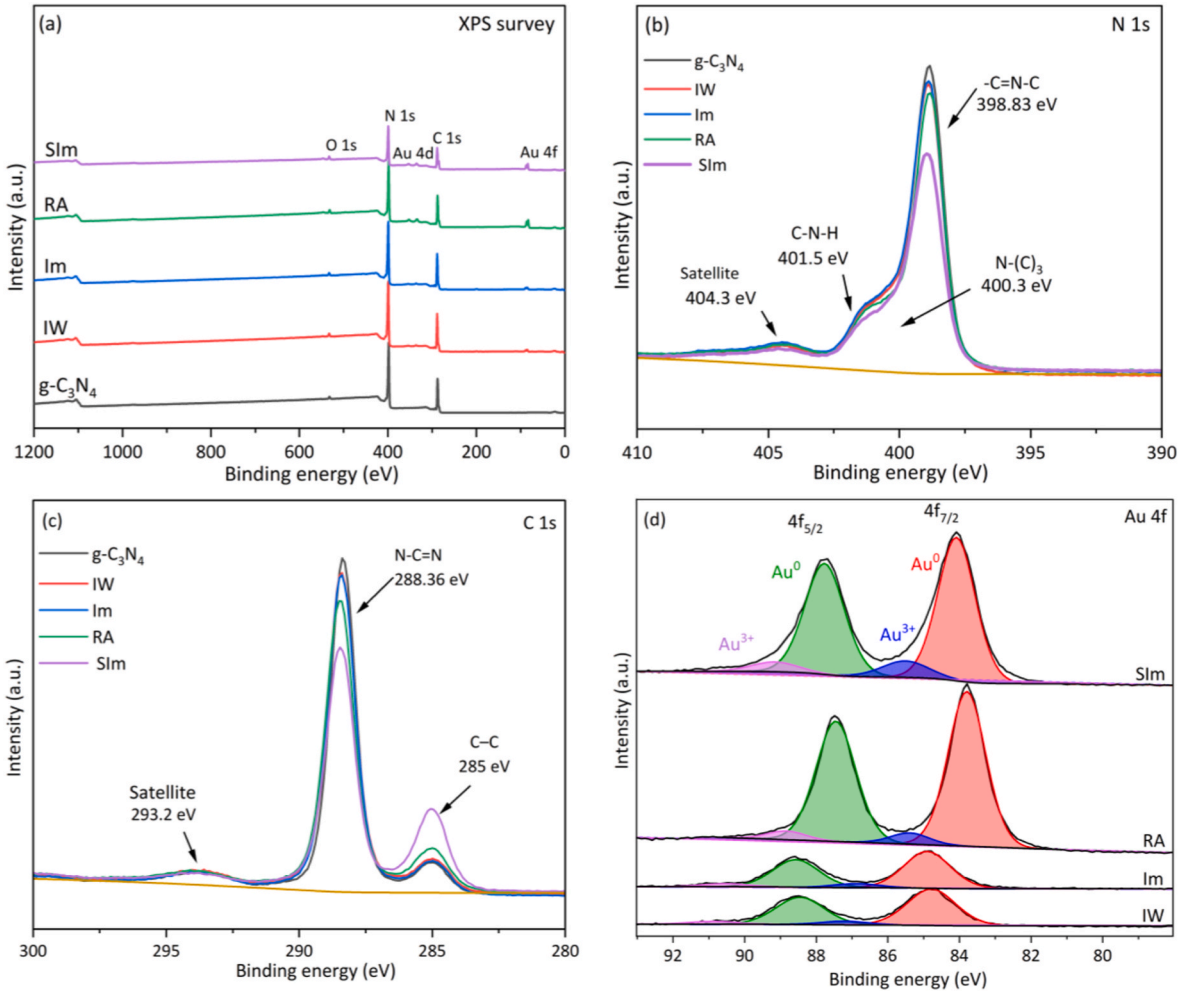

Fig. 4. XPS spectra of g-C_3N_4 and the synthesised 1 wt% Au/g-C_3N_4 catalysts: (a) Survey spectra; (b) High-resolution C 1s; (c) High resolution N 1s spectra; (d) Au 4f spectra.

environment of the g-C_3N_4 support. This decrease became particularly pronounced in the SIm catalyst, probably due to a combination of surface coverage by residual PVA, blockage of surface sites by Au NPs, and potential modifications to the surface chemistry or morphology of g-C_3N_4 [28,29]. Together, these changes in the N 1s and C 1s regions support the idea that modification with Au, especially via the SIm

methodology, alters the electronic environment and surface chemistry of g-C_3N_4.

Fig. 4d shows the high-resolution Au 4f spectra for all Au/g-C_3N_4 catalysts, confirming the coexistence of metallic Au^0 and Au^{3+} species in each sample. The calculated atomic ratio of Au^0/Au^{3+} is comparable across all catalysts (Table S3).

For the IW and Im samples, the Au $4f_{7/2}$ and Au $4f_{5/2}$ peaks are centred at 84.85 eV and 88.58 eV, respectively. The higher binding energies are attributed to the small Au particle size (~2 nm) and strong metal-support interactions [30–32]. The weak Au signal observed by XPS (Fig. 4d and Table S3), despite high bulk Au loading obtained from ICP-MS analysis (Table 1), could reflect the surface sensitivity of XPS (~5–10 nm probing depth) and suggests that a significant fraction of Au exists as highly dispersed ultrasmall species (<0.5 nm), possibly associated with defect or interfacial regions of g-C_3N_4 layers [33]. Additionally, larger Au nanoparticles (~2 nm observed by TEM and detectable by XPS) appear to be located on the external surface of g-C_3N_4. The slight increase in interlayer d-spacing ($\Delta\ d \approx 0.01$ nm) observed by XRD is consistent with local structural distortion, which may be indicative of the presence of sub-nanometric species, although other explanations cannot be excluded. Interestingly, the presence of Au^0 in IW and Im samples, despite the absence of added reducing agents, indicates the spontaneous *in situ* reduction of Au^{3+} occurs *via* nitrogen sites in g-C_3N_4.

Based on the collected data, a plausible formation mechanism for the IW and Im catalysts may be proposed as follows. During preparation, the positively charged Au^{3+} species are likely to be electrostatically attracted toward the negatively charged nitrogen-rich sites of g-C_3N_4. The lone pair of electrons on these nitrogen atoms can also serve as electron donors, facilitating the spontaneous *in-situ* reduction of Au^{3+} to Au^0 under the synthesis conditions, which is thermodynamically reasonable given the highly positive standard reduction potential of the Au^{3+}/Au^0 couple ($E^0 = +1.50$ V vs. NHE) and may account for the formation of ultrasmall Au^0 clusters (<0.5 nm). In the absence of harsh thermal treatment, the mobility of Au species is expected to be limited, and nucleation is tentatively proposed to occur preferentially at surface defect sites or near adjacent g-C_3N_4 layers, consistent with the slight increase in interlayer d-spacing observed by XRD. Limited coalescence of neighbouring clusters could subsequently lead to the formation of ~2 nm nanoparticles as observed by TEM, while Au–N coordination interactions may contribute to stabilising the smaller species and suppressing extensive aggregation. However, further direct characterisation such as EXAFS, *in situ* XRD, or aberration-corrected HAADF-STEM would be needed to confirm this proposed mechanism.

In contrast, the RA and SIm catalysts show more intense and distinct Au 4f signals, with Au^0 $4f_{7/2}$ peaks at 83.09 eV (RA) and 84.15 eV (SIm), and corresponding $4f_{5/2}$ peaks at 86.73 eV and 87.54 eV, respectively. These lower binding energy values are characteristic of larger, surface-exposed metallic Au nanoparticles that exhibit weaker metal-support interactions and more bulk-like Au behaviour [13,30–32,34]. The significantly stronger Au 4f signal intensities confirm the presence of more surface-accessible Au species [32,34]. The binding energy trend strongly correlates with the particle size distribution observed *via* TEM, clearly demonstrating that larger Au nanoparticles exhibit lower binding energy positions.

The optical properties of the catalysts were investigated by UV–Vis diffuse reflectance spectroscopy (DRS) (Fig. 5a). All the samples exhibited an absorption edge at around 450 nm, attributed to the π–π* transitions of the heptazine units, indicating their sensitivity to visible light [35]. Incorporation of Au did not significantly shift the absorption edge of g-C_3N_4. However, the RA and SIm catalysts showed enhanced absorption in the visible region with a broad band centred at 520–530 nm, characteristic of the localized surface plasmon resonance (SPR) of metallic Au nanoparticles which also leads to a change in the colour of the catalysts (Fig. S2) [36]. This plasmonic feature originates from the collective oscillation of conduction band electrons under visible-light excitation [37]. In the IW and Im catalysts, the distinct SPR-related absorption was absent, consistent with the presence of ultrasmall Au species that are below the critical size required to sustain collective plasmon oscillations [38]. Their spectra instead closely resembled that of the unmodified g-C_3N_4, with only a minor increase in baseline absorbance that is due to light scattering [39].

The corresponding Tauc plots (Fig. 5b) revealed the calculated band gap energies (see SI) of 2.78 eV for pristine g-C_3N_4, IW, and Im, 2.76 eV for SIm, and 2.74 eV for RA. The band gap (Eg) values for the composite samples showed a minimal variation compared to the unmodified g-C_3N_4.

3.2. Catalytic performance evaluation against MO degradation

The photocatalytic performances of the as prepared photocatalysts are reported in Fig. 6. The absorption spectrum was recorded at regular intervals throughout the reaction (Fig. S4), and the decomposition of MO was estimated from the decrease in the MO absorbance peak.

To achieve an equilibrium adsorption state and evaluate the adsorption ability of the catalysts, prior to the reaction the MO adsorption under sonication was carried out in the dark for 15 min. From Fig. 6, it can be observed that the catalysts exhibit different adsorption

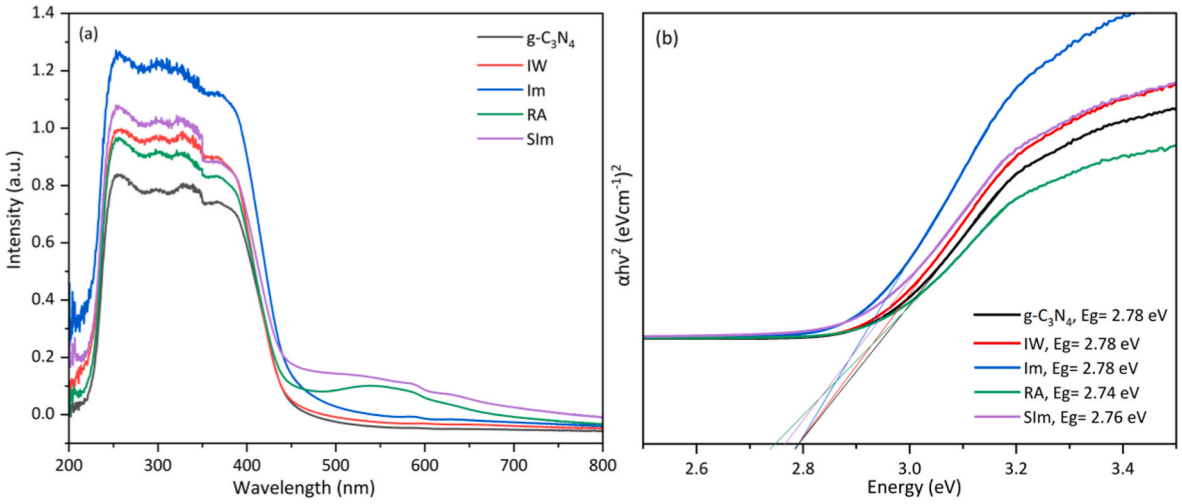

Fig. 5. UV–Vis spectroscopy analysis of g-C_3N_4 and 1 wt% Au/g-C_3N_4 catalysts synthesised by different methods: (a) Diffuse reflectance UV-Vis spectra; (b) Tauc plots to determine the band gap energy.

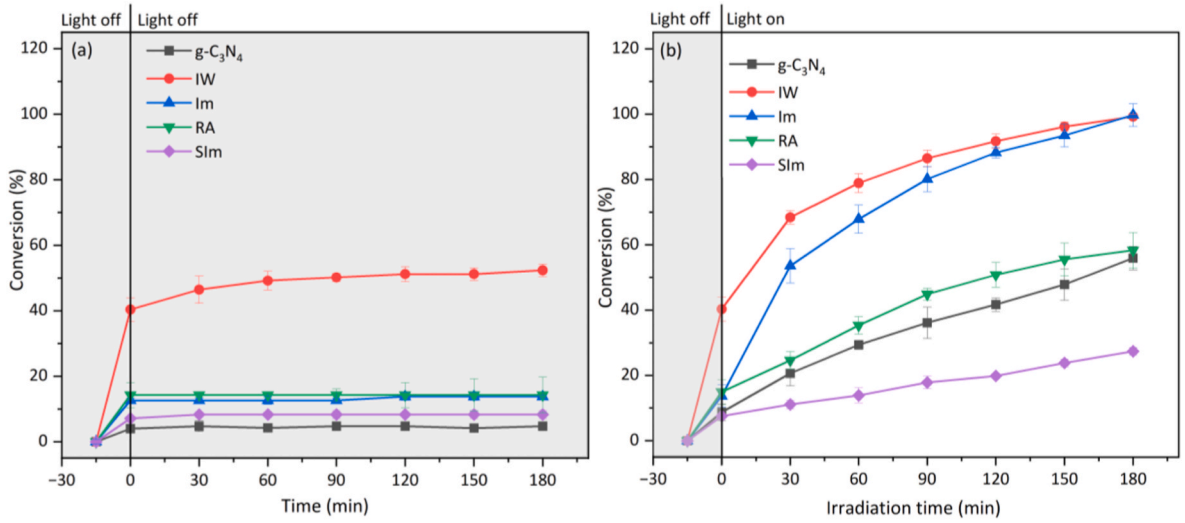

Fig. 6. Photocatalytic MO conversion versus the irritation time for g-C_3N_4 and the Au/g-C_3N_4 samples: (a) in the dark; (b) under vis-light irradiation. Reaction conditions: $[MO]_0 = 10$ mg L^{-1}; solution volume = 50 mL; catalyst dosage = 25 mg; room temperature; open air; stirring at 350 rpm; light source: $420 < \lambda < 700$ nm, intensity = 68 mW cm^{-2}. Prior to reaction, the suspension was sonicated for 15 min.

properties with about 40% adsorption for the IW catalyst and lower adsorption of 10-16% for the other materials. From Fig. 6a, which shows the activity in the dark, after reaching the adsorption/desorption equilibrium, the change in MO signal was not significantly different over the course of their reaction. This demonstrates that the reaction does not occur in the dark and that the adsorption of MO has reached equilibrium after 15 min. Fig. 6b shows the photocatalytic activity under visible light. After 15 min sonication in the dark the light was turned on and the MO absorbance measured at 30 min intervals to determine the photocatalytic activity. The IW and Im photocatalysts show significantly higher MO degradation than the RA and SIm catalysts and the unmodified g-C_3N_4 sample. The highest photocatalytic efficiency was found with the 1 wt% Au/g-C_3N_4 prepared by impregnation and incipient wetness with both showing a degradation efficiency of around 98.5% after 180 min. The unmodified g-C_3N_4 and the RA catalyst both achieved around 60% MO degradation, while the catalyst prepared by SIm was found to have the lowest activity, achieving just 22% conversion, considerably lower than the unmodified g-C_3N_4.

While the comprehensive characterisation data provide a logical basis for the superior photocatalytic activity of the Im and IW catalysts, several observations prompt further investigation. Notably, the higher adsorption capacity of the IW catalyst and the rapid onset of photocatalytic activity in both IW and Im samples imply that additional mechanisms may be involved. Three hypotheses can be proposed: (i) the elevated activity of Im and IW may be related to the leaching of Au^{3+} species from the catalyst surface; (ii) the adsorption of MO on IW could be influenced by surface impurities, as this sample did not undergo additional treatments such as washing or calcination; (iii) the enhanced performance of IW and Im may arise from sub-surface or intercalated ultrasmall Au species, which could facilitate more effective charge separation or induce internal electric fields within the g-C_3N_4 structure. Further experiments were carried out as described below to test these hypotheses.

Although the IW and Im catalysts were synthesised without the use of external reducing agents, TEM analysis confirmed the presence of Au nanoparticles on the g-C_3N_4 surface, suggesting there is an *in-situ* reduction of the Au^{3+} precursor to metallic Au^0, potentially facilitated by the electron-rich support. However, XPS analysis indicated the presence of residual Au^{3+} species, implying incomplete reduction and the coexistence of both oxidation states (Fig. 4, Table S3). These observations led to two working hypotheses: (i) the high photocatalytic activity may result from a synergistic effect between Au^0 and Au^{3+}; and (ii) partial leaching of Au^{3+} during the reaction may contribute to homogeneous catalytic degradation. To evaluate these possibilities, additional control experiments was conducted.

A set of experiments was designed to evaluate the photocatalytic activity of Au^{3+} ions in solution, using $HAuCl_4{\cdot}3H_2O$ as the homogeneous gold source, both in the absence and presence of g-C_3N_4 under visible light irradiation for 180 min (Fig. 7). The amount of Au^{3+} introduced into the solution stoichiometrically matched the gold content in the solid Au/g-C_3N_4 catalysts (IW and Im), corresponding to the amount of Au in 25 mg of catalyst (i.e., 40.3 μL of a 12.4 mg mL^{-1} $HAuCl_4{\cdot}3H_2O$ solution).

Fig. 7 shows the photocatalytic degradation of MO under visible light irradiation under different test conditions. In the absence of a catalyst (photolysis), no measurable MO conversion was observed, confirming the photostability of the dye under the applied illumination. The homogeneous solution containing $HAuCl_4$ also exhibited no activity, with

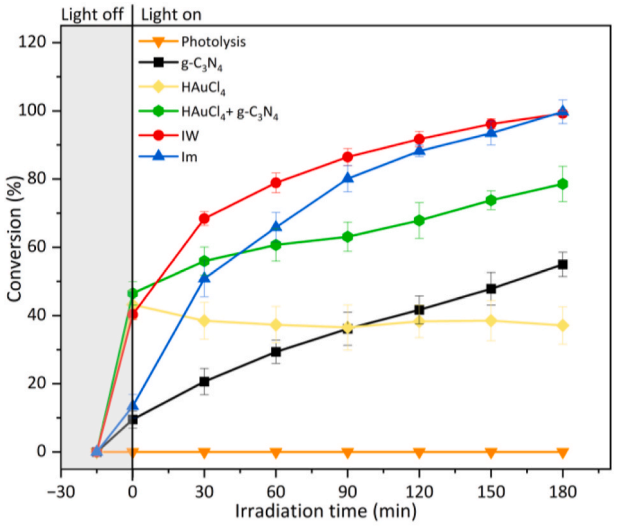

Fig. 7. MO Degradation efficiency under visible light. Reaction conditions: $[MO]_0 = 10$ mg L^{-1}; solution volume = 50 mL; catalyst dosage = 25 mg; room temperature; open air; stirring at 350 rpm; light source: $420 < \lambda < 700$ nm, intensity = 68 mW cm^{-2}. Prior to reaction, the suspension was sonicated for 15 min.

MO conversion remaining constant over the full 180 min period, indicating that Au^{3+} ions alone do not contribute significantly to photocatalytic degradation under these conditions. When g-C_3N_4 was used as the photocatalyst, the MO conversion reached 59.5% after 180 min, demonstrating moderate photocatalytic activity. In the presence of both $HAuCl_4$ and g-C_3N_4, the conversion increased to 78.5% ($HAuCl_4$ + g-C_3N_4), which initially appeared to suggest enhanced performance. However, this apparent improvement was largely due to a strong increase in the initial MO adsorption induced by the Au precursor. After correcting this non-photocatalytic contribution (Fig. 7, $HAuCl_4$ + g-C_3N_4 - adsorption), the net photocatalytic activity of the $HAuCl_4$/g-C_3N_4 mixture was comparable to that of g-C_3N_4 alone, while the IW, and Im exhibited a markedly superior performance, achieving full MO conversion after 180 min. This suggests that Au^{3+}, whether alone or in combination with g-C_3N_4, did not account for the high photocatalytic activity observed in the Au/g-C_3N_4 catalysts.

To determine if Au^{3+} leached from the catalyst, the reaction solution was analyzed by ICP-MS following the reaction, and the data are reported in Table 2.

The results reveal a low presence of Au^{3+} in the post-reaction media, with 0.0146 and 0.0314 ppm present in the solution for the catalysts prepared respectively by IW and Im. To test whether these species contributed to the activity, blank reactions were run with these concentrations of Au^{3+} added to the reaction mixture (Fig. S5). No conversion of MO was found at the detected leaching concentrations for IW and Im catalysts during the irradiation time, indicating that the Au^{3+} leaching from the catalysts had no effect on methyl orange degradation.

Parameters that could affect MO adsorption were investigated and compared using the IW and Im catalysts in the dark. A plot of MO conversion with time-on-line showed that there was a high initial adsorption when $HAuCl_4$ and a mixture of g-C_3N_4 + $HAuCl_4$ were added to the MO which was comparable to the adsorption observed previously for the IW catalyst (Fig. S6). As $HAuCl_4$ was found to increase the adsorption of MO in the presence of g-C_3N_4, additional experiments were carried out to investigate the role of protons and chloride ions on the decrease in MO signal, observed in the UV-Vis spectra, by adding HCl and NaCl with the g-C_3N_4 and the results are shown in Fig. 8a. As observed in Fig. 8a and Table 3, there was an adsorption of around 46% when $HAuCl_4.3H_2O$ was added, with and without g-C_3N_4, whereas MO adsorption was about 10% with g-C_3N_4 alone, which confirms that the presence of $HAuCl_4.3H_2O$ influences the adsorption. The addition of NaCl to the solution did not affect the adsorption, ruling out chloride ion involvement in the process. However, HCl addition led to increased MO adsorption (37%), suggesting that the pH of the solution, rather than chloride ions, was responsible for the enhanced adsorption. To test this hypothesis, the pH of the MO solution was measured and compared to the pH with the different additives following the sonication step in the dark and the measured pH was plotted against the amount of MO adsorption (Fig. 8b).

As it can be seen from Fig. 8b, the pH has a strong influence on MO adsorption, with the adsorption increasing as the pH is lowered. According to a related study, the adsorption of methyl orange onto a catalyst surface is subject to modulation by the pH of the medium, as the adsorption process is intricately linked to both the charge of the catalyst surface and the charge of the dye molecule [40]. At lower pH levels, the catalyst surface acquires a positive charge, attracting the negatively charged methyl orange molecules, resulting in an high adsorption. Conversely, at higher pH levels, the catalyst surface becomes negatively charged, leading to repulsion of the negatively charged methyl orange molecules and consequently a reduction in adsorption [40,41].

In this study, the IW synthesis methodology using $HAuCl_4$ does not have a washing step, leaving residual acid in the catalyst that can dissolve into the MO solution leading to a decrease in the pH during the reaction. To assess the impact of surface-adsorbed species on catalytic activity, the IW catalyst was rigorously washed with deionized water and ethanol to remove any residual acid left on the catalyst after the synthesis The resulting material, referred to as WIW, was subsequently evaluated for its catalytic performance (Fig. 9).

The washing step was found to significantly reduce MO adsorption on the catalyst surface after 15 min sonication in the dark. Interestingly, despite this reduction in adsorption, the photocatalytic activity of the washed catalyst remained high and comparable to the Im catalyst, achieving an MO degradation of approximately 98.9% after 180 min. Furthermore, ICP-MS analysis revealed that the WIW catalyst contained 0.90 ± 0.05 wt% of gold, closely aligning with the intended loading. This result demonstrates negligible gold loss during washing, confirming that Au^0 species remain securely anchored to the g-C_3N_4 support through strong metal–support interactions, probably arising from Au–N coordination at defect sites and favourable electrostatic interactions.

Table 2
ICP-MS result for reaction solution after 180 min reaction time towards the photodegradation of MO.

Sample Name	Au^{3+} ppm (mg L^{-1})	The gold leaching (%)
Au/g-C_3N_4 (IW)	0.0146 ± 0.0005	0.3%
Au/g-C_3N_4 (Im)	0.0314 ± 0.0006	0.6%

3.3. Charge carrier dynamics in IW and Im catalysts

With control experiments confirming that the enhanced photocatalytic activity of the IW and Im catalysts was not attributable to residual Au^{3+} species, and the unusually high MO adsorption on the IW sample resolved through washing, the role of charge carrier dynamics was explored as good photocatalysts are expected to have a high charge transfer rate and a low recombination rate of photoexcited holes and electrons [42,43]. It is hypothesised that the bimodal Au distribution (ultrasmall species and surface-bound nanoparticles) collectively enhances photocatalytic activity by facilitating electron trapping, suppressing charge recombination, and promoting local charge redistribution within the g-C_3N_4 framework. To investigate this process, photoluminescence (PL), photocurrent response and electrochemical impedance spectroscopy (EIS) Nyquist plots were used to investigate the generation of electron-hole pairs under light irradiation, charge carrier recombination effect and charge transfer resistance.

PL was performed to determine the recombination rate of photogenerated electron–hole pairs in the catalysts. Fig. 10 shows the PL spectra of g-C_3N_4, WIW and Im catalysts and the peak intensity reflects the recombination rate of photoexcited holes and electrons. Under excitation at 350 nm, all samples exhibited an emission peak at ~460 nm. Pristine g-C_3N_4 showed higher PL intensity than the Au/g-C_3N_4 materials. The reduced intensities observed for the IW and Im catalysts, by approximately 24% and 35%, respectively, indicate suppressed radiative recombination of photogenerated charge carriers. This behaviour suggests enhanced interfacial charge separation and electron transfer across the Au/g-C_3N_4 interface [36].

Fig. 11a shows the photocurrent responses for g-C_3N_4 and Im for four light-on/light-off cycles under irradiation of visible light. Both the WIW and Im catalysts displayed photocurrent densities of ~0.10–0.11 μA, which are approximately 2.7 times higher than that of g-C_3N_4 (~0.04 μA), indicating improved charge separation and transport efficiency. While the photocurrent of the unmodified g-C_3N_4 decreased over repeated on/off light cycles, both WIW and Im maintained stable signals, indicating improved photostability. This enhancement is attributed to improved interfacial charge separation at the Au/g-C_3N_4 interface, where metallic Au^0 nanoparticles act as electron sinks, facilitating charge transfer and effectively suppressing electron–hole recombination without significantly altering the intrinsic band structure of g-C_3N_4 [36, 42–44].

EIS was employed to assess the charge transfer resistance of the catalysts compared to g-C_3N_4 (Fig. 11b). The Nyquist plots reveal that both WIW and Im catalysts exhibit markedly smaller semicircular arcs

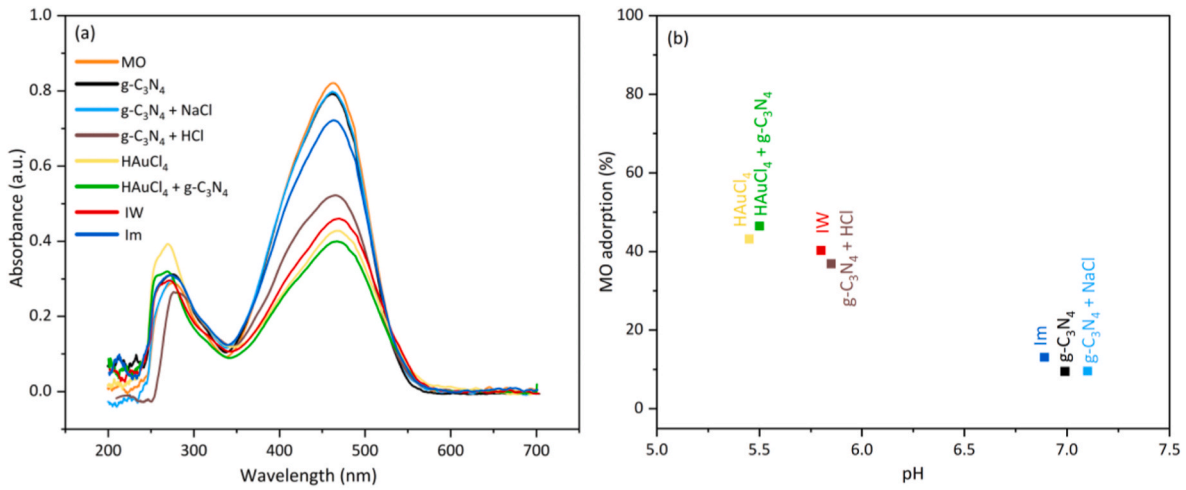

Fig. 8. (a) UV–vis spectra of MO solution without irradiation in the presence of different control samples, (b) pH reading of reaction medium for the controls at time 0-min.

Table 3
Effect of different additives on the pH and methyl orange (MO) adsorption efficiency in the dark.

	MO	$g\text{-}C_3N_4$	$g\text{-}C_3N_4$ + NaCl	$g\text{-}C_3N_4$ + HCl	$HAuCl_4$	$HAuCl_4$ + $g\text{-}C_3N_4$	IW	Im
pH	7	6.9	6.7	5.6	5.5	5.4	5.6	7
Absorbance (%)	-	9.6 ± 0.7	9.5 ± 0.5	37 ± 3.2	43 ± 4.1	46 ± 3.4	40.3 ± 5.1	13.5 ± 2.5

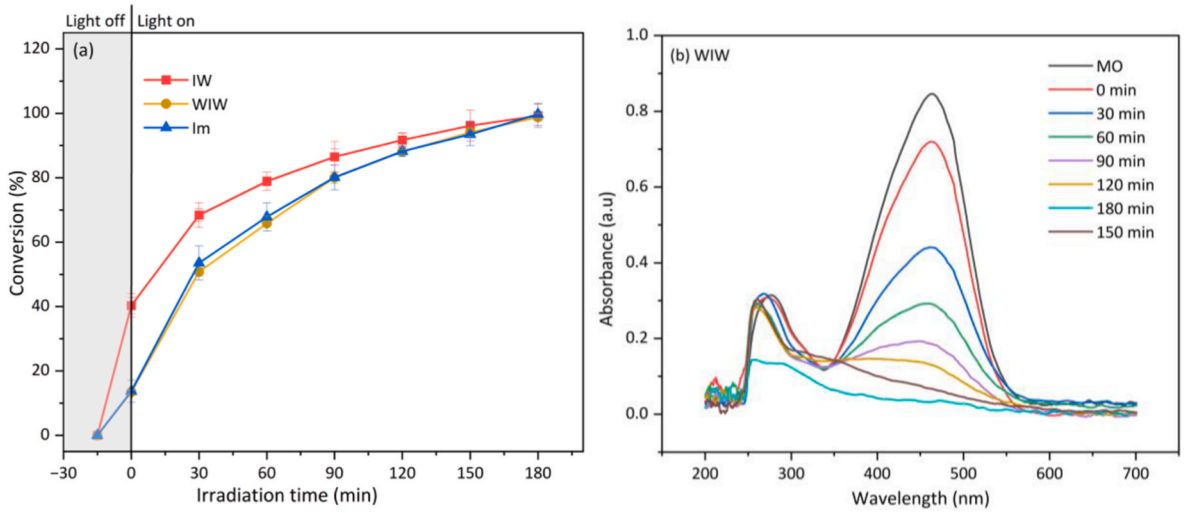

Fig. 9. (a) Photocatalytic MO degradation under visible light irradiation for IW, WIW, and Im samples, and (b) time-dependent UV–Vis absorption spectra during MO degradation using WIW catalyst. Reaction conditions: $[MO]_0 = 10$ mg L^{-1}; solution volume = 50 mL; catalyst dosage = 25 mg; room temperature; open air; stirring at 350 rpm; light source: $420 < \lambda < 700$ nm, intensity = 68 mW cm^{-2}. Prior to reaction, the suspension was sonicated for 15 min.

compared to pristine $g\text{-}C_3N_4$, indicating reduced interfacial charge-transfer resistance. This reflects more efficient separation and transport of photoinduced charge carriers [36,42–44].

The combined results from PL, photocurrent response, and EIS analyses confirm that Au incorporation significantly enhances charge separation and interfacial electron transfer, thereby suppressing recombination and contributing directly to the improved photocatalytic performance.

3.4. Kinetic study of MO photocatalysis

To enable reliable performance comparison, photocatalytic activity was evaluated through kinetic analysis rather than simple degradation percentages. The MO degradation kinetics were fitted to a pseudo-first-order model, using Eq. (3) [26].

$$ln\,(C_0 / C_t) = kt \quad (3)$$

where k is the first-order kinetic rate constant (min^{-1}), C_0 is the initial pollutant concentration, and C_t is the pollutant concentration at time t. For visualization, the data are plotted as $-\,ln\,(C_0/C_t)$ versus time (Fig. 12b), where the gradient corresponds to the rate constant k. From (Fig. 12b–Table S4), all samples exhibit excellent linearity ($R^2 > 0.95$), confirming that the reaction follows first-order kinetics under the employed conditions.

The kinetic results of MO degradation (Fig. 12b–Table S4), show that the WIW activity was not affected by the washing step as the rate

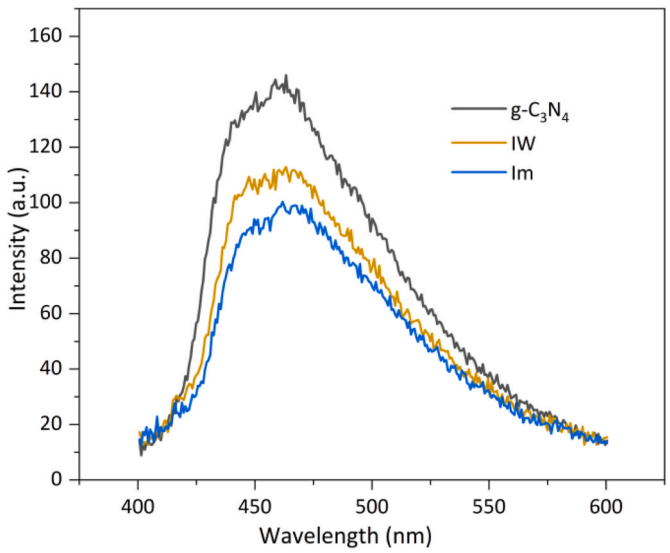

Fig. 10. Steady-state photoluminescence spectra of g-C_3N_4 and Au/g-C_3N_4 samples.

constant of IW (1.8×10^{-2} min^{-1}) and the WIW (2.047×10^{-2} min^{-1}) were found to be similar and, together with that of Im (2.05×10^{-2} min^{-1}), were approximately 4-fold higher than the unmodified g-C_3N_4 (0.5×10^{-2} min^{-1}). The ~4-fold enhancement in activity can therefore be attributed to the bimodal Au size distribution we propose, comprising ultrasmall clusters (<0.5 nm) embedded within the g-C_3N_4 framework and highly dispersed surface-exposed nanoparticles (~2 nm), which collectively improve charge separation and suppress recombination through efficient electron trapping, while maintaining excellent surface accessibility for interfacial MO degradation. The comparable activity of WIW and Im is particularly noteworthy. Despite the additional overnight stirring step in the Im preparation, prolonged contact time did not further enhance Au dispersion or metal-support interaction under the present conditions. This implies that Au deposition onto g-C_3N_4 is largely governed by electrostatic adsorption and spontaneous reduction, both of which proceed efficiently in either method. From a practical standpoint, the WIW method is therefore preferable as it achieves equivalent performance through a simpler and less time-consuming protocol. The catalyst prepared by RA exhibited a slightly lower rate constant (0.36×10^{-2} min^{-1}) compared to unmodified g-C_3N_4, and this poorer performance could be due to the relatively large Au particle size in this catalyst. The SIm catalyst demonstrated the lowest activity ($k = 0.13 \times 10^{-2}$ min^{-1}), even lower than g-C_3N_4. This can be attributed to the presence of PVA, which is used as a stabilising agent in the sol immobilisation method. Villa *et al.* demonstrated that PVA can sterically hinder access to active Au sites by physically blocking the catalyst surface, thereby reducing catalytic activity. In the present system, this steric blocking effect likely limits the accessibility of MO molecules to the active Au– g-C_3N_4 interface, contributing to the observed decrease in photocatalytic performance [28].

A comparison of the present Au/g-C_3N_4(WIW) catalyst with a range of recently reported Au–g-C_3N_4 systems (Table S5) highlights the effectiveness and practicality of the synthesis approach used in this work. Although the reported materials employ diverse preparation strategies, light sources, and pollutant models, the overall trends clearly demonstrate that many rely on higher catalyst dosages, more complex synthesis routes, or intensified illumination conditions to achieve high degradation efficiencies. In contrast, the Au/g-C_3N_4 catalyst synthesised *via* a simple washed incipient-wetness method delivers complete MO degradation under low-power LED irradiation, placing it among the most efficient and accessible systems listed. The combination of straightforward preparation, low metal loading, and strong photocatalytic response positions this material as a state-of-the-art Au/g-C_3N_4 photocatalyst, offering both high performance and practical scalability compared with existing literature examples. We also investigated the reusability of the catalysts and found that the WIW catalyst retained 90% of the activity when used recovered and washed before being used in a second reaction (Fig. S11). Post reaction characterisation by XRD, TEM and XPS suggested that an increase in the Au particle size was the reason for the decrease in performance (Figs. S12–S14).

3.5. Investigation of the photocatalytic reaction mechanism

3.5.1. Radical scavenging tests

To identify the dominant radicals responsible for the photodegradation of the MO pollutants over the 1 wt% Au/g-C_3N_4 catalysts, scavenger experiments were performed with the WIW catalyst and unmodified g-C_3N_4 to understand the role of the Au NPs. Potassium iodide (KI), tertiary butyl alcohol (TBA), and benzoquinone (pBQ) were used as scavengers for (h^+), ($^{\bullet}OH$), and ($O_2^{\bullet-}$) respectively.

The degradation behaviour of methyl orange (MO) over the unmodified g-C_3N_4 and the WIW catalyst in the presence of the different reactive species scavengers, along with the corresponding kinetic rate constants is shown in Fig. 13. For g-C_3N_4, the addition of p-benzoquinone (pBQ), a superoxide radical ($O_2^{\bullet-}$) scavenger, resulted in a decrease in MO degradation efficiency, with the rate constant dropping from 0.5×10^{-2} to 0.3×10^{-2} min^{-1}. This modest inhibition suggests that $O_2^{\bullet-}$

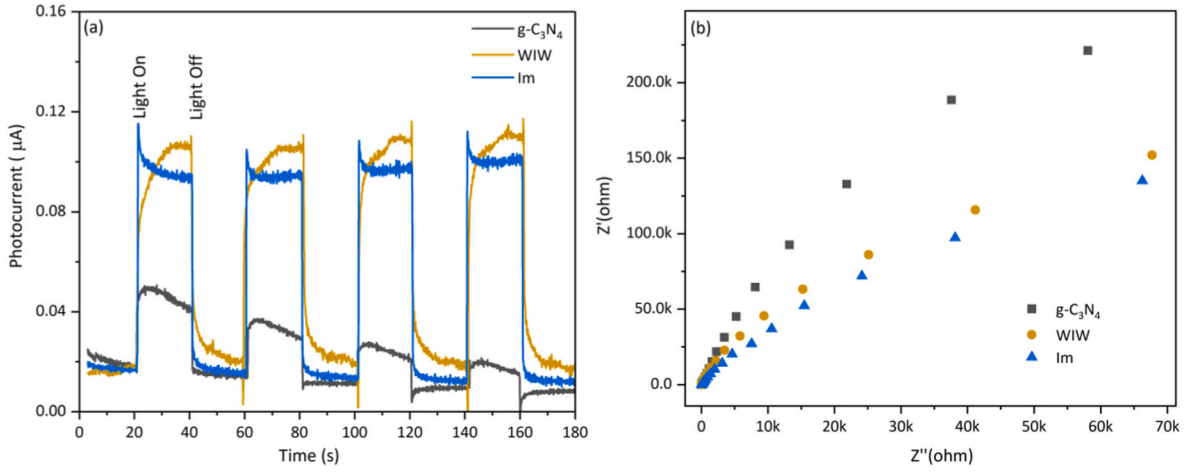

Fig. 11. (a) Photocurrent response over time under visible light in 0.5 M Na_2SO_4, and (b) Nyquist plot from electrochemical impedance spectroscopy (EIS) for g-C_3N_4, WIW, and Im catalysts.

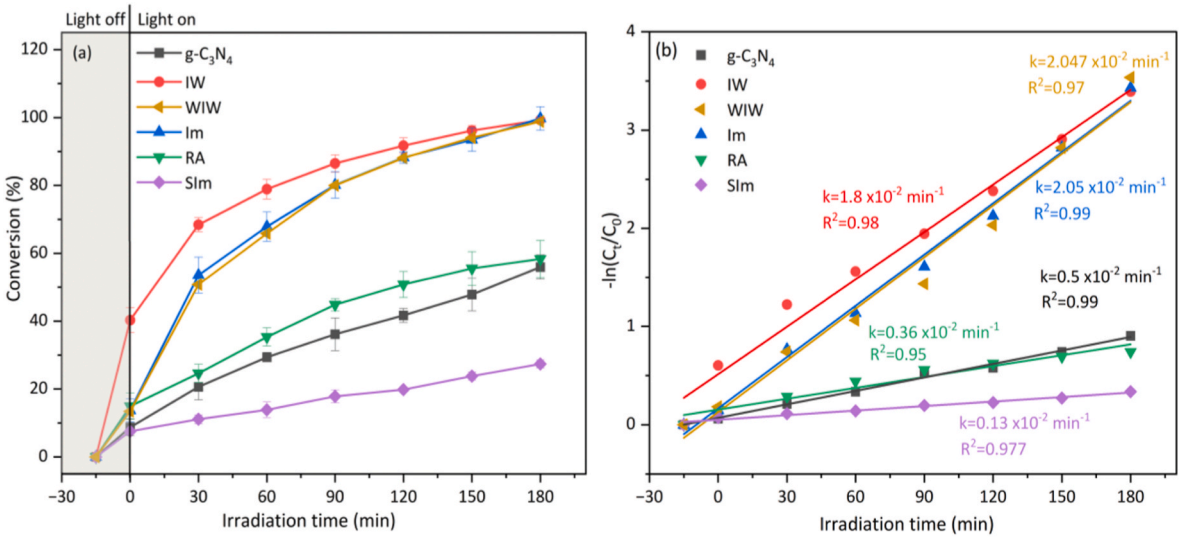

Fig. 12. (a) Photocatalytic degradation under vis-light irradiation for g-C_3N_4 and the Au/g-C_3N_4 catalysts; (b) their kinetic rate constants. Reaction conditions: $[MO]_0$ = 10 mg L^{-1}; solution volume = 50 mL; catalyst dosage = 25 mg; room temperature; open air; stirring at 350 rpm; light source: 420 < λ < 700 nm, intensity = 68 mW cm^{-2}. Prior to reaction, the suspension was sonicated for 15 min.

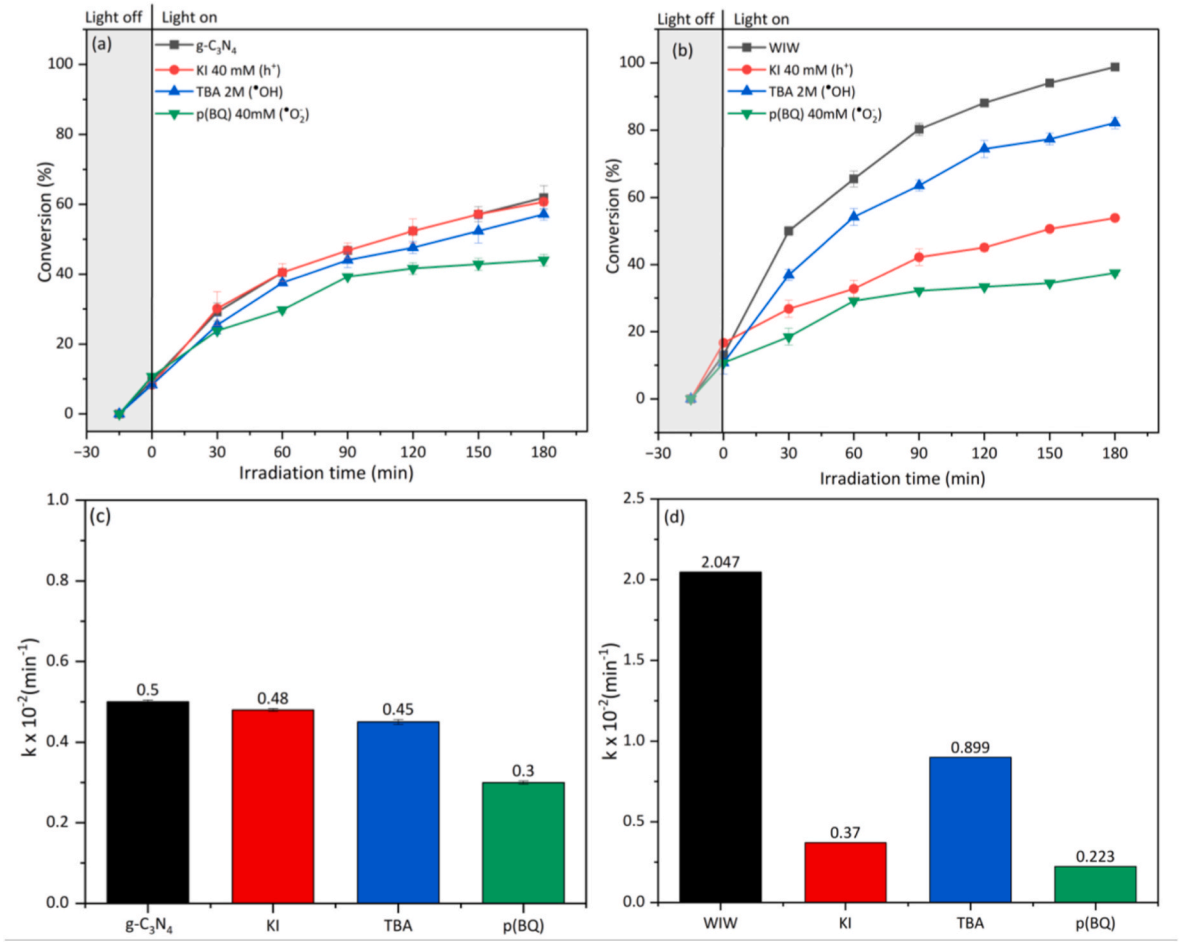

Fig. 13. Trapping experiments for the photodegradation of MO in the presence of different scavenger reagents: (a) with g-C_3N_4; (b) with WIW; (c) kinetic rate constants for g-C_3N_4; (d) kinetic rate constants for WI. Reaction conditions: $[MO]_0$ = 10 mg L^{-1}; solution volume = 50 mL; pH = 7; catalyst dosage = 25 mg; $[TBA]_0$ = 2.0 M, and $[BQ]_0 = [KI]_0$ = 40 mM; room temperature; open air; stirring at 350 rpm; light source: 420 < λ < 700 nm, intensity = 68 mW cm^{-2}. Prior to reaction, the suspension was sonicated for 15 min.

plays an important role in the photocatalytic activity of g-C_3N_4. The introduction of tert-butanol (TBA), a hydroxyl radical (•OH) scavenger,

caused a small reduction ($k = 0.45 \times 10^{-2}\ min^{-1}$), indicating a limited contribution from $^{\bullet}OH$ species. Notably, the presence of potassium iodide (KI), a hole (h^+) scavenger, had negligible impact on the photocatalytic performance ($k = 0.48 \times 10^{-2}\ min^{-1}$), suggesting that photogenerated holes do not significantly contribute to MO degradation in the absence of Au. In contrast, there is a markedly different response for the WIW catalyst upon scavenger addition. The presence of pBQ led to a sharp decline in photocatalytic activity, with the rate constant decreasing from 2.05×10^{-2} to $0.223 \times 10^{-2}\ min^{-1}$, confirming the key role of $O_2^{\bullet-}$ in the degradation process. KI also caused significant inhibition ($k = 0.37 \times 10^{-2}\ min^{-1}$), highlighting the enhanced involvement of photogenerated holes. The effect of TBA was more moderate ($k = 0.899 \times 10^{-2}\ min^{-1}$), indicating a secondary but non-negligible role for $^{\bullet}OH$ radicals. A similar trend was observed for the Im catalyst (Fig. S8), further supporting the conclusion that the presence of small Au nanoparticles in g-C_3N_4 photocatalysts leads to increase the e^-/h^+ pair recombination time, which enables more efficient participation of both holes and $O_2^{\bullet-}$ radicals in the photocatalytic degradation of MO. This is supported by PL, photocurrent, and EIS measurements.

3.5.2. *Proposed photocatalytic mechanism*

The proposed photocatalytic mechanism for MO degradation over Au/g-C_3N_4 (WIW and Im) is illustrated in Fig. 14 and summarized in Equations (4)–(8). Under visible light irradiation, g-C_3N_4 generates electron–hole pairs (Equation (4)). The photogenerated electrons, further facilitated by metallic Au acting as an electron sink, reduce surface-adsorbed oxygen to superoxide radicals ($O_2^{\bullet-}$) (Equation (5)), which may subsequently yield H_2O_2 and $^{\bullet}OH$ via sequential reduction steps (Equations (6) and (7)). The relatively minor role of $^{\bullet}OH$ is consistent with the valence band position of g-C_3N_4 (+1.63 eV, XPS, Fig. S9), which is insufficient to directly oxidise water to $^{\bullet}OH$ (+2.39 eV). The generated reactive species, primarily $O_2^{\bullet-}$ and h^+, with a secondary contribution from $^{\bullet}OH$, collectively drive MO degradation into CO_2, H_2O, and other mineralisation products (Equation (8)) [45].

$$Au/g\text{-}C_3N_4 + h\nu \rightarrow e^- + h^+ \quad (4)$$

$$e^- + O_2 \rightarrow O_2^{\bullet-} \quad (5)$$

$$O_2^{\bullet-} + 2H^+ + e^- \rightarrow H_2O_2 \quad (6)$$

$$H_2O_2 + H^+ + e^- \rightarrow H_2O + {}^{\bullet}OH \quad (7)$$

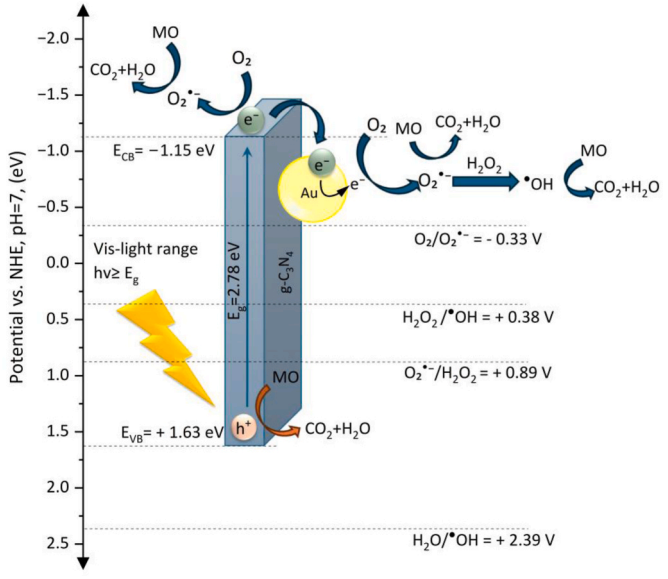

Fig. 14. Proposed photocatalytic MO degradation mechanism over WIW/Im catalysts.

$$O_2^{\bullet-} + {}^{\bullet}OH + h^+ + MO \rightarrow \text{intermediates} \rightarrow CO_2 + H_2O + \text{other products} \quad (8)$$

4. Conclusions

This study demonstrates that the preparation method plays a critical role in controlling the structural, optical, and catalytic properties of Au/g-C_3N_4 photocatalysts. While all catalysts contained similar Au loadings, their photocatalytic activities varied markedly with the preparation method, with distinct differences in gold nanoparticle size, dispersion, and metal–support interactions observed depending on the synthesis route. We suggest that the catalysts prepared by washed incipient wetness (WIW) and impregnation (Im) produced bimodal Au distributions: ultrasmall species (<0.5 nm) intercalated within interlayers that account for the increase in stacking distance between the g-C_3N_4 observed indirectly by the changes in the (002) reflection in XRD, and ~2 nm nanoparticles on surfaces, as confirmed by TEM, ICP, and XPS analyses. These strong metal–support interactions suppressed plasmon resonance but enhanced charge transfer, enabling the IW and Im catalysts to achieve a fourfold higher activity than bare g-C_3N_4, completing methyl orange degradation within 180 min. Additionally, the solution pH was found to significantly influence the initial adsorption of methyl orange on the catalyst surface, further affecting overall degradation efficiency. The mechanism for the degradation was determined based on scavenger experiments, the dominant reactive species were superoxide radicals ($O_2^{\bullet-}$), hydroxyl radicals ($^{\bullet}OH$), and photogenerated holes (h^+). Taken together, the results highlight that beyond gold loading, the synthesis method governs nanoparticle characteristics, interfacial chemistry, and adsorption behaviour, ultimately determining photocatalytic performance. Owing to its straightforward synthesis, effective Au dispersion, and strong activity, the WIW catalyst stands out as a promising candidate for visible-light-driven water purification. Although methyl orange was selected as a typical azo dye model pollutant in this study, the enhanced charge separation and interfacial electron transfer achieved with Au/g-C_3N_4 catalysts are expected to be general features of this system. It is therefore anticipated that this strategy could be extended to the degradation of other organic pollutants susceptible to visible-light photocatalysis, including other azo dyes, phenolic compounds, and pharmaceutical contaminants, highlighting the broader potential of reducing-agent-free Au deposition for sustainable water treatment applications.

This work underscores the importance of rational catalyst design and provides valuable insights for the development of sustainable photocatalysts for environmental remediation.

CRediT authorship contribution statement

Mshaal Almalki: Conceptualization, Data curation, Formal analysis, Investigation, Methodology, Validation, Visualization, Writing – original draft. **Ouardia Akdim:** Investigation, Methodology, Supervision, Validation, Writing – review & editing. **James S. Hayward:** Investigation, Methodology, Supervision. **Jennifer K. Edwards:** Conceptualization, Methodology, Resources, Supervision. **Jonathan K. Bartley:** Conceptualization, Data curation, Methodology, Project administration, Resources, Writing – review & editing.

Declaration of competing interest

The authors declare that they have no known competing financial interests or personal relationships that could have appeared to influence the work reported in this paper.

Acknowledgements

MA extend her appreciation to Kingdom of Saudi Arabia and Imam Abdulrahman bin Faisal University for funding her PhD studies. XPS data were collected at the CCI by David Morgan, and PL analysis was performed by Prof. Bo Hou's team, at the School of Physics and Astronomy, Cardiff University.

Appendix A. Supplementary data

Supplementary data to this article can be found online at https://doi.org/10.1016/j.mtsust.2026.101348.

Data availability

Data presented in this study are openly available free of charge through the Cardiff University Research Portal (https://doi.org/10.17035/cardiff.31819645).

References

[1] D.M. Schultz, T.P. Yoon, Science (1979) 343, https://doi.org/10.1126/science.1239176.
[2] Y. Shen, A.J. Dos Santos-Garcia, M. José, M. De Vidales, Processes 9 (2019) 66, https://doi.org/10.3390/pr9010066.
[3] J. Feng, D. Zhang, H. Zhou, M. Pi, X. Wang, S. Chen, ACS Sustain. Chem. Eng. 6 (2018) 6342–6349.
[4] C. Xu, P.R. Anusuyadevi, C. Aymonier, R. Luque, S. Marre, Chem. Soc. Rev. 48 (2019) 3868–3902.
[5] W. Hussain, H. Malik, M.A. Khan, M.J. Iqbal, R.A. Hussain, R. Shoukat, Y. Khan, A. Badshah, M. Sulaman, H. Li, Semicond. Sci. Technol. 34 (2019) 095015.
[6] Z. Yong, J. Ren, H. Hu, P. Li, S. Ouyang, H. Xu, D. Wang, J. Nanomater. (2015), https://doi.org/10.1155/2015/821986.
[7] J. Vasiljević, I. Jerman, B. Simončič, Polymers 13 (2021) 2568, https://doi.org/10.3390/polym13152568.
[8] Y. Li, B. Zhang, H.-J. Lü, P.H. Linh, P.D. Chung, L.T.M. Oanh, N.V. Khien, T. N. Bach, L.T. Thai, L.T. Hang, N.M. Hung, D.V. Thanh, Semicond. Sci. Technol. 37 (2022) 13.
[9] W.-J. Ong, L.-L. Tan, Y.H. Ng, S.-T. Yong, S.-P. Chai, Chem. Rev. 116 (2016) 7159–7329.
[10] S. Ye, R. Wang, M.Z. Wu, Y.P. Yuan, Appl. Surf. Sci. 358 (2015) 15–27.
[11] S. Patnaik, S. Martha, S. Acharya, K.M. Parida, Inorg. Chem. Front. 3 (2016) 336–347.
[12] S. Samanta, S. Martha, K. Parida, ChemCatChem 6 (2014) 1453–1462.
[13] M. Faisal, M. Jalalah, F.A. Harraz, A.M. El-Toni, A. Khan, M.S. Al-Assiri, Ceram. Int. 46 (2020) 22090–22101.
[14] Y. Liu, H. Zhang, Y. Lu, J. Wu, B. Xin, Catal. Commun. 87 (2016) 41–44.
[15] M. Faisal, M. Jalalah, F.A. Harraz, A.M. El-Toni, A. Khan, M.S. Al-Assiri, Ceram. Int. (2020), https://doi.org/10.1016/j.ceramint.2020.05.250.
[16] W. Zhang, L. Zhou, H. Deng, J. Mol. Catal. Chem. 423 (2016) 270–276.
[17] T. Alizadeh, S. Nayeri, N. Hamidi, RSC Adv. 9 (2019), https://doi.org/10.1039/c9ra00982e.
[18] A. Aljuaid, M. Almehmadi, A.A. Alsaiari, M. Allahyani, O. Abdulaziz, A. Alsharif, J. A. Alsaiari, M. Saih, R.T. Alotaibi, I. Khan, Molecules 28 (2023) 3199.
[19] M. Zhang, Y. Yang, X. An, J. Zhao, Y. Bao, L. an Hou, J. Hazard Mater. 424 (2022) 127424.
[20] B. Yue, Q. Li, H. Iwai, T. Kako, J. Ye, Sci. Technol. Adv. Mater. 12 (2011) 034401.
[21] F. Fina, S.K. Callear, G.M. Carins, J.T.S. Irvine, Chem. Mater. 27 (2015) 22.
[22] D.P. Hashim, N.T. Narayanan, J.M. Romo-Herrera, D.A. Cullen, M.G. Hahm, P. Lezzi, J.R. Suttle, D. Kelkhoff, E. Muñoz-Sandoval, S. Ganguli, A.K. Roy, D. J. Smith, R. Vajtai, B.G. Sumpter, V. Meunier, H. Terrones, M. Terrones, P. M. Ajayan, Sci. Rep. 2 (2012) 363, https://doi.org/10.1038/srep00363.
[23] S.S. Godipurge, S. Yallappa, N.J. Biradar, J.S. Biradar, B.L. Dhananjaya, G. Hegde, K. Jagadish, G. Hegde, Enzym. Microb. Technol. 95 (2016) 174–184.
[24] Y. Pan, K. Qiao, C. Ning, X. Wang, Z. Liu, Z. Chen, Nanomaterials 13 (2023) 2964.
[25] J. Yang, X. Zhang, C. Xie, J. Long, Y. Wang, L. Wei, X. Yang, J. Electron. Mater. (2020), https://doi.org/10.1007/s11664-020-08654-1.
[26] M. Faisal, A.A. Ismail, F.A. Harraz, S. Al-Sayari, A.M. El-Toni, M. Al-Assiri, Mater. Des. (2016), https://doi.org/10.1016/j.matdes.2016.03.019.
[27] S. Martha, A. Nashim, K.M. Parida, J. Mater. Chem. A (2013), https://doi.org/10.1039/c3ta10851a.
[28] A. Villa, D. Wang, G.M. Veith, F. Vindigni, L. Prati, Catal. Sci. Technol. 3 (2013) 3036.
[29] H. Huang, D. Yu, F. Hu, S.C. Huang, J. Song, H.Y. Chen, L.L. Li, S. Peng, Angew. Chem. Int. Ed. 61 (2022) e202116068.
[30] M. Caux, H. Ménard, Y.M. Alsalik, J.T.S. Irvine, H. Idriss, Phys. Chem. Chem. Phys. 21 (2019) 15974–15987, https://doi.org/10.1039/C9CP02241D.
[31] M. Benedet, A. Gasparotto, G.A. Rizzi, D. Barreca, C. Maccato, Surf. Sci. Spectra 29 (2022) 024001, https://doi.org/10.1116/6.0002028.
[32] M.Y. Smirnov, A.V. Kalinkin, A.V. Bukhtiyarov, I.P. Prosvirin, V.I. Bukhtiyarov, J. Phys. Chem. C 120 (2016) 10419–10426, https://doi.org/10.1021/acs.jpcc.6b02090.
[33] D.N.G. Krishna, J. Philip, Appl. Surf. Sci. Adv. 12 (2022) 100332.
[34] J. Radnik, C. Mohr, P. Claus, Phys. Chem. Chem. Phys. 5 (2003) 172–177, https://doi.org/10.1039/B207290D.
[35] A.B. Jorge, David, J. Martin, M.T.S. Dhanoa, A.S. Rahman, N. Makwana, J. Tang, A. Sella, F. Cora, S. Firth, J.A. Darr, P.F. Mcmillan, J. Phys. Chem. C 117 (2013) 8.
[36] Z. Guo, F. Dai, H. Yin, M. Zhang, J. Xing, L. Wang, Colloid Interface Sci Commun 48 (2022) 100615.
[37] J. Chen, Y. Chen, J. Shuai, X. Chen, D. Zhang, X. Lu, X. Fang, B. Zou, X. Yu, F. Zhao, W. Feng, J. Alloys Compd. 1009 (2024) 176938, https://doi.org/10.1016/j.jallcom.2024.176938.
[38] T.G. Schaaff, M.N. Shafigullin, J.T. Khoury, I. Vezmar, R.L. Whetten, W.G. Cullen, P.N. First, C. Gutiérrez-Wing, J. Ascensio, M.J. Jose-Yacamán, J. Phys. Chem. B 101 (1997) 7885–7891.
[39] S. Link, M.A. El-Sayed, J. Phys. Chem. B 103 (1999) 4212–4217.
[40] Arteaga-Jiménez, A.I. Caudana-Campos, A.L. García-García, E. Hernández-Zapata, M.A. Vidales-Hurtado, MRS Adv 4 (2019) 3399–3405.
[41] M. Tsuji, K. Matsuda, M. Tanaka, S. Kuboyama, K. Uto, N. Wada, H. Kawazumi, T. Tsuji, H. Ago, J.I. Hayashi, Chem. Select. 3 (2018) 1432–1438.
[42] Y. He, L. Zhang, X. Wang, Y. Wu, H. Lin, L. Zhao, W. Weng, H. Wan, M. Fan, RSC Adv. 4 (2014) 13610–13619.
[43] X. Lin, S. Du, C. Li, G. Li, Y. Li, F. Chen, P. Fang, Catal. Lett. 150 (2020) 1898–1908.
[44] P. Song, S. Sun, J. Cui, X. Zheng, S. Liang, Appl. Surf. Sci. 568 (2021) 150986.
[45] D.A. Armstrong, R.E. Huie, S. Lymar, W.H. Koppenol, G. Merényi, P. Neta, D. M. Stanbury, S. Steenken, P. Wardman, Bioinorg. React. Mech. 9 (2013) 59–61.